Soil Dynamics and Earthquake Engineering 94 (2017) 193–203

Contents lists available at ScienceDirect

Soil Dynamics and Earthquake Engineering

journal homepage: www.elsevier.com/locate/soildyn

Existing prefab R/C industrial buildings: Seismic assessment and supplemental damping-based retrofit

Stefano Sorace[a,*], Gloria Terenzi[b]

[a] Polytechnic Department of Engineering and Architecture, University of Udine, Via delle Scienze 206, 33100 Udine, Italy
[b] Department of Civil and Environmental Engineering, University of Florence, Via S. Marta 3, 50139 Florence, Italy

ARTICLE INFO

Keywords:
Prefab reinforced concrete structures
Industrial buildings
Non-seismically designed structures
Performance assessment
Seismic retrofit
Supplemental damping
Dissipative braces

ABSTRACT

A research study on prefab reinforced concrete buildings designed with older Technical Standards is presented in this paper, where attention is focused on hall-type industrial structures. A representative case study, which includes the main sources of seismic vulnerability, is examined in detail. The possible rigid rotation of the bottom end zone of columns, which are encased in smooth socket-type foundations, and the frictional contact between the neoprene pads situated on top of the columns and the terminal zone of the roof girders are modelled in time-history assessment analyses. Initially carried out by assuming an elastic behaviour of columns, the analyses highlight unsafe response conditions under seismic action scaled at the basic design earthquake level, and near-collapse caused by the loss of support of several girders from the neoprene pads at the maximum considered earthquake level. A second step of the analyses, where plastic behaviour of columns is investigated by incorporating fiber-type plastic hinges at their bottom end sections, shows a remarkable ductility demand, as well as potential collapse induced by the complete loss of support of girders. The high lateral displacements of columns may also cause failure of the fastenings of the connected cladding panels, likely to result in their overturning-induced collapse. Based on these data, a supplemental damping-based retrofit hypothesis is suggested, consisting in the installation of dissipative braces equipped with pressurized fluid viscous spring-dampers. The protective system allows attaining a completely undamaged response of structural and non-structural members, and therefore meeting the requirements of the Immediate Occupancy limit state, up to the maximum considered earthquake level.

1. Introduction

Prefab reinforced concrete (R/C) buildings designed with older Technical Standards have shown poor response capacities during low-to-moderate earthquakes in the past two decades [1–7]. The main causes of the damage surveyed in these structures — sometimes involving partial or complete collapse — are the failure of roof purlins-to-roof girders, roof tiles-to-roof girders, girders-to-columns, floor slabs-to-beams, beams-to-columns, columns-to-foundation and cladding panels-to-columns connections; the low ductility of columns; the insufficient in-plan stiffness of the roof and floor systems; and the unfavourable interactions between cladding panels and connected columns or beams. In the case of single-storey precast R/C structures, which are the most common typology of industrial buildings in the Mediterranean area, collapse is mainly caused by the loss of support of the roof elements from roof-girders and/or of the latter from columns, due to the absence or insufficient size of mechanical connectors. Indeed, the most widely used joint type is a thin neoprene pad or a steel plate, usually 10 mm thick in both cases, located at the interface between roof members and girders, as well as of girders and columns, without steel dowel restrainers. These connections absorb lateral loads purely by means of the frictional mechanism occurring on the faces of the bearing pads/plates. When the maximum earthquake-induced displacements of the supported elements exceed the length of the corresponding pad/plate side, unseating of their terminal zones follows, causing significant portions of the building to collapse. Other remarkable sources of seismic vulnerability are the connections between precast concrete cladding panels and structural elements, constituted by steel bars, angles or fasteners. Failure of these elements determines the detachment of the panels, and their consequent over-turning towards the exterior of the buildings. Severe damage or collapse of panels is also frequently determined by high displacements of the joined columns, induced by the plasticization of their bottom end sections, and/or by rigid elastic rotations in the same zones, when columns are simply encased and grouted in smooth socket-type foundations.

* Corresponding author.
E-mail addresses: stefano.sorace@uniud.it (S. Sorace), gloria.terenzi@unifi.it (G. Terenzi).

http://dx.doi.org/10.1016/j.soildyn.2017.01.023
Received 25 September 2016; Received in revised form 1 December 2016; Accepted 16 January 2017

A study on single-storey hall-type industrial R/C buildings is presented in this paper, where a structure including the above-mentioned sources of seismic vulnerability is examined as representative case study. The structure was built in a small industrial town near Udine, Friuli-Venezia Giulia region, Italy in the late 1980s, when this municipality was classed as a non-seismic zone. Later, the new classification of the Italian territory prescribed by the 2008 edition of the national Technical Standards [8] included the municipality in a moderate seismic zone.

In view of the considerations above, the structural assessment analysis of the building is carried out by simulating the effects of rigid rotation of the column base sections and the frictional contact between neoprene pads placed on top of columns and the lower face of the bearing zone of roof girders. The results highlight unsafe response conditions of columns under seismic action scaled at the basic design earthquake (BDE) level, and near-collapse at the maximum considered earthquake level (MCE), caused by the loss of support of several girders from the neoprene pads. The incorporation of plastic hinges at the bottom end sections of columns, implemented at a second step of the analysis, shows a noticeable ductility demand and high lateral displacements capable of determining the collapse of girders, for loss of support from the internal columns, and cladding panels, due to the failure of their fastenings to the perimeter columns.

In order to substantially improve the seismic performance evaluated in current conditions, a “global” retrofit hypothesis (i.e. aimed at reducing the overall seismic vulnerability of the building, rather than specifically constraining local damage mechanisms) is designed and evaluated. The retrofit intervention consists in adding a dissipative bracing system incorporating pressurized fluid viscous spring-dampers. The response in protected configuration results to be elastic and characterised by low lateral displacements, assessing the attainment of the Immediate Occupancy performance level, up to the maximum considered earthquake level.

2. Geometrical and structural characteristics of the building

As mentioned above, the structure was designed in the late 1980s, in compliance with the 1986 edition of the Italian Technical Standards, for gravity and wind loads only. The drawings of the front and side façades, the longitudinal and transversal sections and the plan are shown in Fig. 1, along with the *X* and *Y* axes of the reference Cartesian coordinate system (*Z* being the vertical axis). As highlighted in these drawings, the plan is rectangular, with sides of 79.5 m in longitudinal direction, parallel to *X*, and 42.8 m in transversal direction, parallel to *Y*. The structure is double-hall type, constituted by 18 triangle-shaped pre-stressed R/C girders, named G1 through G18 in the plan of Fig. 1, with cross section height varying from 620 mm to 1700 mm and 20.9 m net span. The girders are situated on nine transversal alignments of three R/C columns each — numbered C1A-C1B-C1C through C9A-C9B-C9C in Fig. 1 — along *Y*. The neoprene pads found between the end sections of the girders and the top of columns are 10 mm thick, with plan size of 370 mm along *X* and 250 mm (perimeter columns) or 120 mm (central columns) along *Y*. The three outer sides of the girder end zones are 20 mm wider than the pad sides. The fourth side of the pads is found at a 20 mm distance from the side of the column top section. Based on these geometrical data, in *Y* direction the loss of support of the girders from pads and columns occurs for displacements of 230 mm and 250 mm (perimeter columns), and 140 mm and 160 mm (central columns).

The column alignments are placed at a mutual distance of 9.8 m. The height of the roof top is equal to 10.03 m, whereas the height of the façades, constituted by a continuous curtain of cladding panels, is equal to 10.2 m. The roof is made of a set of pre-stressed R/C purlins with 500 mm high T-shaped section, composed of a 80 mm wide web and a 50 mm thick upper slab. The section is reduced to one half in the end zones, so as to form a Gerber-type connection with the girders, to which the purlins are fastened by means of threaded Ø 16 steel bars. This solution was originally adopted to absorb and share wind loads, and allows obtaining a rigid diaphragm function of the roof with respect to seismic forces too. Columns have a mutual section with sides of 600 mm along *X* and 700 mm along *Y*, up to the top of the corbels supporting the overhead travelling cranes; the side parallel to *Y* is reduced to 500 mm over the corbels. The four cranes are situated at an height of 7 m along the longitudinal direction. The longitudinal reinforcement of columns is constituted by 4 ∅20+8 ∅16 bars, reduced to 4 ∅20 bars in the portion over the corbels. The transversal reinforcement consists of ∅8 stirrups placed at a mutual distance of 125 mm. The bottom end zone of each column is grouted with cement mortar into a smoothed socket-type R/C foundation, consisting of a 500 mm high footing slab with base section of (2800×2900) mm×mm, and a 850 mm high hollow-core body with external sides of 1500 mm along *X* and 1600 mm along *Y*, and thickness of the four constituting walls varying from 450 mm, at the base, to 400 mm, on top. The column height over the socket foundation is equal to H=8.18 m. The cladding panels are connected to the columns by means of Ø16 bolts screwed to “Halfen”-type steel channel-profiles, at their horizontal ends; to a continuous R/C foot edge-beam (which also connects the socket foundations along the perimeter of the building), at the bottom end; and to the lateral purlins of the roof, on top. The panels-purlins joints are situated at a 8.77 m height from the column base, named H_{cp} in the following, i.e. 1.43 m below the top end section of the panels. The pinned connections of the panels, widely used in prefab R/C industrial buildings in Italy, simply transfer their self-weight to the joined elements, but do not allow the panels to contribute to the lateral stiffness of the building. As a consequence, the presence of the panels is simulated in the finite element analyses only in terms of dead loads and corresponding seismic inertial masses, without structural interactions with the columns and the purlins. The total seismic weight of the building is equal to about 1800 t. The dead plus live gravitational loads distributed on the girders are equal to 35 kN/m.

The mechanical properties of concrete and steel, as well as the reinforcement details have been drawn from the original design documentation, as no testing campaigns were carried out on the structural members. These documents highlight that the compressive cube strength of concrete, f_c, is equal to 35 MPa for the columns and the other non pre-stressed structural members, and 48 to MPa for the pre-stressed girders and purlins. The yield stress, f_y, and strength, f_u, of the reinforcing steel for non pre-stressed members are equal to 430 MPa, and 540 MPa. The nominal yield stress at 0.1 residual strain, $f_{y,p,0.1}$, and the strength, $f_{u,p}$, of the harmonic-type steel for pre-stressed members are equal to 1700 MPa, and 1950 MPa.

3. Finite element model of the structure

3.1. Mesh geometry and modal parameters

The finite element model of the structure, a view of which is displayed in Fig. 2, was generated by SAP2000NL software [9]. The model is constituted by 920 frame elements reproducing the roof purlins and girders, and the columns. The rotations of the base sections of columns and the frictional neoprene-concrete contact are modelled by means of additional link-type elements, as discussed in Sections 3.2 and 3.3.

Fixed-end conditions were assumed for the base sections of the columns in the modal analysis carried out at the first step of the assessment study. The results show four main vibration modes, the first of which is purely translational along the weakest direction *X*, with a period of 1.69 s and an effective modal mass (EMM) equal to 88.2% of the total seismic mass. The third mode is purely translational along *Y*, with period of 1.31 s and EMM equal to 91.3%. The second and fourth mode are purely rotational around the vertical axis *Z*, with periods of 1.38 s and 1.24 s, and EMMs equal to 84.1% and 8.5%, giving a

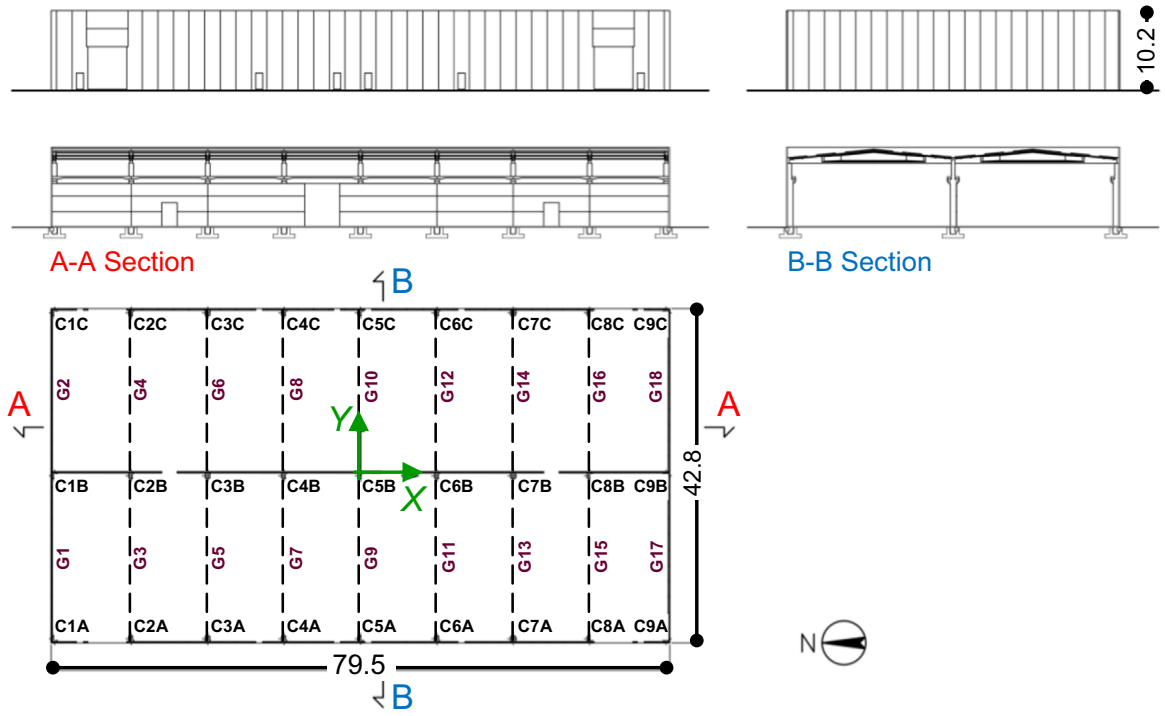

Fig. 1. Main and side façades, sections and plan (dimensions in meters) of the building.

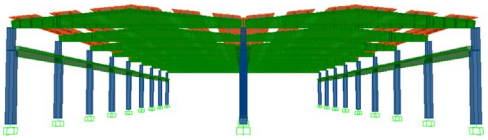

Fig. 2. View of the finite element model.

summed modal mass of 92.6%. The remaining mass fractions required to activate 100% of the total seismic mass along X and Y (equal to 11.8% — X, and 8.7% — Y) and around Z (7.4%) are contributed by several secondary modes, all associated to the local deformation of single elements and/or limited portions of the model, rather than to its overall response.

3.2. Rotation model of the base section of columns

Studies carried out on socket-type foundations of sway precast frame structures [10] highlighted that the connection of the encased columns can be modelled as a fixed-end joint when, by referring to the drawing on the left in Fig. 3, the column embedment depth, h_e, is at least 1.5 times as large as the column side, s, in the considered vertical plan. For smaller depths, the local failure in compression of the concrete mortar filling the peripheral gap between column and hollow-core cavity walls, generally caused by moderate-to-severe earthquakes [4,5,7,10], reduces the constraining action towards lateral displacements of the column end-zone, often determining non negligible rotations of the base section. Therefore, the rotational constraint decreases as the embedment depth ratio h_e/s does, with $1 \le h_e/s < 1.5$ representing the range of semi-rigid to rigid connections, and $h_e/s < 1$ the range of semi-rigid to flexible connections, respectively [10].

The condition $h_e/s \ge 1.5$ is not met in the examined building, where h_e is equal to 800 mm (obtained by subtracting the thickness of the grout pad over the bottom footing slab, b_g=50 mm, from the h_c=850 mm height of the hollow-core body walls), that is, 1.14 and 1.33 times the s values of 700 mm and 600 mm along Y and X. In view of these data, which correspond to h_e/s values falling in the $1 \le h_e/s < 1.5$ range for both axes, the possible rotations of the base section of columns were considered in the analysis with the aim of evaluating their effects on the seismic performance of the building. The rotations were simulated by incorporating an elastic rotational spring at the column base in both vertical plans, as sketched in the scheme on the right in Fig. 3, referred to the Y-Z plan. The stiffness of the springs placed in the X-Z plan, $k_{\varphi Y}$ (allowing for rotations around Y), and the Y-Z plan, $k_{\varphi X}$ (allowing for rotations around X), is calculated as follows:

$$k_{\varphi Y} = \alpha \frac{E_c I_Y}{H_p} \quad (1)$$

$$k_{\varphi X} = \alpha \frac{E_c I_X}{H_p} \quad (2)$$

where: E_c=Young modulus of concrete, I_Y, I_X=moments of inertia of the column section computed with respect to Y and X, H_p=column

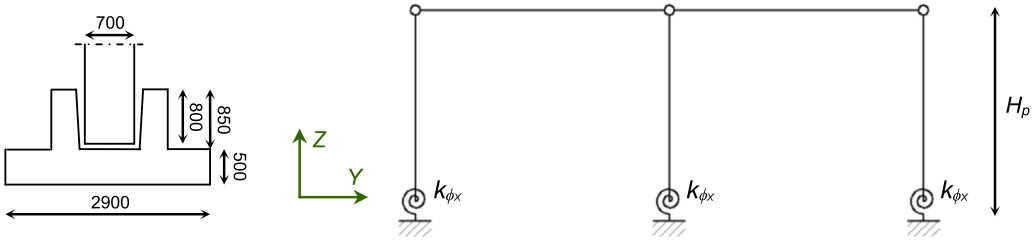

Fig. 3. Vertical section of a foundation, and scheme of the structure in the Y-Z plan including relevant elastic rotational springs at the column feet.

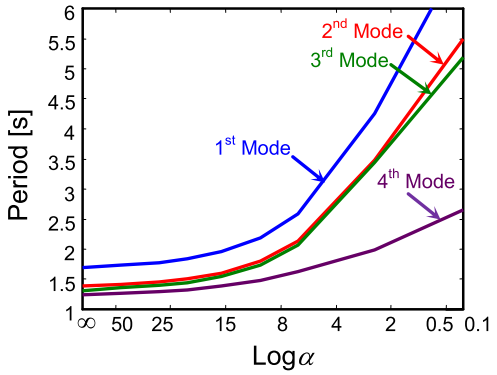

Fig. 4. Vibration periods of the first four modes as a function of α (logarithmic scale).

height measured from the net mid-height of the hollow-core body to the column top, i.e. H_p=H+h_e/2, and α=stiffness modulation coefficient. Relations (1) and (2) are similar to the expressions adopted for semi-rigid column–foundation connections of steel sway structures [11], whose flexibility can notably influence the response to lateral forces of the structural system too. A parametric analysis was carried out by assuming thirteen α values, in addition to fixed-end conditions (equivalent to α=∞), and namely: 50, 40, 30, 20, 15, 10, 8, 6, 4, 2, 1, 0.5 and 0.1 (α=0 was not considered as it corresponds to a structural hypostatic condition when the roof girders-neoprene pads frictional contact, discussed in the next Section, is in the slip stage during dynamic response, thus producing no horizontal translational constraint). Relevant $k_{\varphi Y}$ and $k_{\varphi X}$ values, calculated by means of (1) and (2), were assigned to the springs incorporated in the finite element model, and a corresponding set of modal analyses was developed. The results are summarised in the graph of Fig. 4, where the values of the periods of the above-mentioned four main modes are plotted as a function of *log*α (logarithmic scale is adopted for compact representation). As shown in the graph, the periods increase rather linearly in the α range [∞,10], corresponding to semi-rigid to rigid connections [11], with variations ranging from 12%, on the first period, to 6%, on the fourth period. The correlation becomes remarkably non-linear below α=10, with a progressively more accentuated growth of periods, consistently with the fact that this sub-range represents near-hinge to hinge conditions. For α=0.1 the periods are over 3 times greater (first through third mode) and about 2 times greater (fourth mode) than the corresponding values for α=∞. All modal shapes are unchanged up to α=10, whereas the shapes of the second and third mode tend to reciprocally merge in the sub-range α < 10.

Based on these data and by considering that the embedment depth ratio is included in the $1 \le h_e/s < 1.5$ range for both axes, it seems reasonable to limit the time-history analyses to the field of semi-rigid to rigid connections, thus evaluating the response in the α range [∞,10], as discussed in Section 4.

3.3. Frictional model of neoprene pad-roof girder contact

The sliding contact between the neoprene pads and the terminal zones of the supported roof girders was simulated by the special "Friction Isolator" link element available in the library of SAP2000NL program. This is a stick-slip element with coupled friction properties for the deformations along the two reference local axes in plan, governed by a Coulomb-type hysteretic law, and "gap"-type (i.e. no tension) behaviour in vertical direction. The value of the friction coefficient, μ, was fixed by referring to the results of extensive experimental studies [12] carried out on neoprene-to-concrete connections with geometrical characteristics that are typical of the bearing pads adopted in Italian precast R/C structures from 1960s through 1980s, among which the standard 10 mm thickness mentioned in the Introduction. The analytical relation interpolating the test data is:

$$\mu = 0.1 + \frac{0.055}{\sigma_v} \quad (3)$$

with σ_v=compressive normal stress, expressed in MPa. The application field of (3) is for σ_v ranging from 1.5MPa to 5 MPa. The normal stress values computed for the bearings of the case study building are: $\sigma_{v,tl}$=2.2 MPa (terminal girders on lateral columns); $\sigma_{v,tc}$=2.8 MPa (terminal girders on central columns); $\sigma_{v,il}$=3.6 MPa (internal girders on lateral columns); $\sigma_{v,ic}$=4.9 MPa (internal girders on central columns). Substituting these values in (3), $\mu(\sigma_{v,tl}$=2.2 MPa)=0.125, $\mu(\sigma_{v,tc}$=2.8 MPa)=0.122, $\mu(\sigma_{v,il}$=3.6 MPa)=0.118 and $\mu(\sigma_{v,ic}$=4.9 MPa)=0.111 are obtained. By considering that the differences among the four μ values are at most equal to about 10%, and in view of the inherent approximations of relation (3), a unified coefficient was adopted in the analysis for all bearings, equal to the intermediate $\mu(\sigma_{v,il})$=0.118 value.

4. Performance assessment analysis in current conditions

4.1. Earthquake levels

The performance evaluation enquiry was carried out for the four reference seismic levels fixed in the Italian Standards [8], that is, Frequent Design Earthquake (FDE, with 81% probability of being exceeded over the reference time period V_R); Serviceability Design Earthquake (SDE, with 50%/V_R probability); Basic Design Earthquake (BDE, with 10%/V_R probability); and Maximum Considered Earthquake (MCE, with 5%/V_R probability). The V_R period is fixed at 50 years. By referring to topographic category T1 (flat surface), and C-type soil (deep deposits of dense or medium-dense sand, gravel or stiff clay from several ten to several hundred meters thick), the resulting peak ground accelerations for the four seismic levels referred to the site of the building are as follows: 0.075g (FDE), 0.096g (SDE), 0.254g (BDE), and 0.313g (MCE), for the horizontal motion components; and 0.015g (FDE), 0.022g (SDE), 0.1g (BDE), and 0.151g

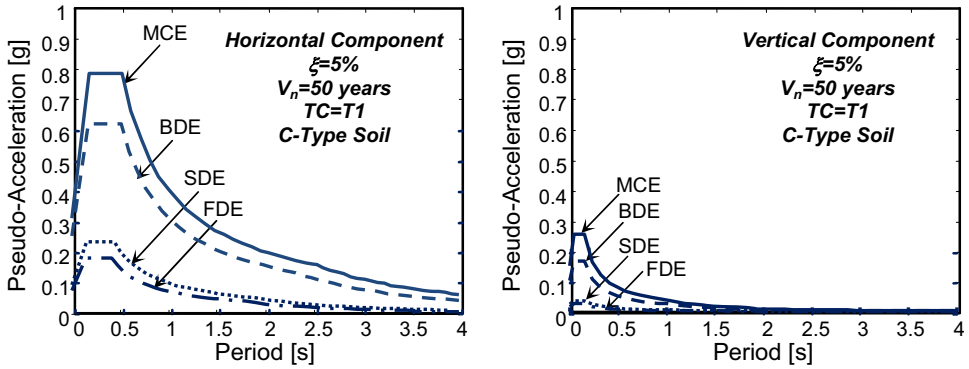

Fig. 5. Normative pseudo-acceleration elastic response spectra — horizontal and vertical components.

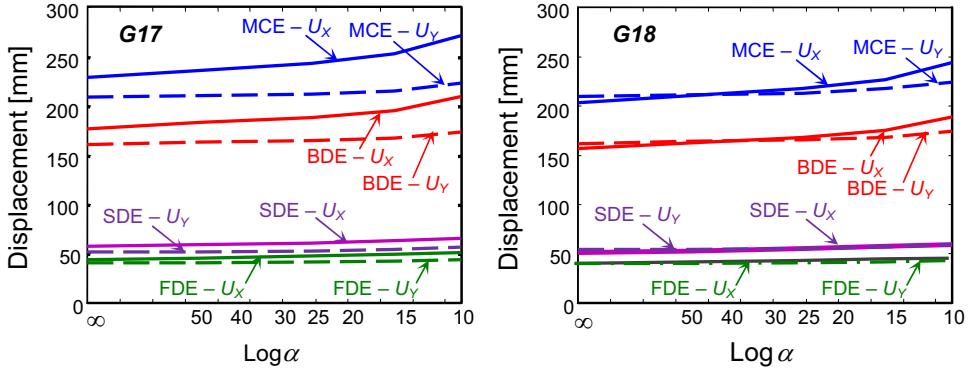

Fig. 6. Maximum displacements of the left end sections of roof girders G17 and G18 as a function of α in the [∞,10] range (absolute values – logarithmic scale).

(MCE), for the vertical component. Relevant elastic pseudo-acceleration response spectra at linear viscous damping ratio ξ=5% are plotted in Fig. 5.

4.2. Time-history verification and performance assessment analysis – Elastic model of columns

Time-history analyses were developed by assuming artificial ground motions as inputs, generated in families of seven by SIMQKE-II software [13] from the spectra above, both for the horizontal components (two families) and the vertical one (one family). As required by the Italian Standards for structures including horizontal members with span greater than 20 m, in each time-history analysis the accelerograms were applied in groups of three simultaneous components, i.e. two horizontal components, with the first one selected from the first generated family of seven motions, and the second one selected from the second family, plus the vertical component.

The results of the analyses carried out with the columns modelled as elastic elements are summarised in Figs. 6–9. The absolute values of the maximum horizontal displacements along X (U_X) and Y (U_Y) of the left end sections of roof girders G17 and G18 — borne by columns C9A and C9B, respectively — are plotted as a function of α in Fig. 6, for all earthquake levels and α belonging to the [∞,10] range corresponding to semi-rigid to rigid connections discussed in Section 3. Column C9A was selected as representative of the four corner columns of the building (C1A, C1C, C9A and C9C), and C9B of the two central columns situated on the façades (C1B and C9B). The displacements obtained for the girders placed on the inner column alignments, i.e. C2A–C2B–C2C through C8A–C8B–C8C, progressively decrease in X and Y as compared to the façade alignments C1A–C1B–C1C and C9A–C9B–C9C, with a maximum reduction of about 16% (U_X) and 30% (U_Y) for the central alignment C5A–C5B–C5C, as a consequence of the torsional response of the structure in plan. It is noted that the displacements of the end sections of the girders practically coincide with the ones of the panels-purlins joints, located only 150 mm above, due to the presence of rigid connections between purlins and girders. Therefore, the displacements of the end sections of the latter can be assumed as equal to the drifts of the cladding panels measured at their top joint level, situated at the above-mentioned H_{cp} height of 8.77 m. Based on this assumption, by expressing the results in terms of drift ratio (i.e. the ratio of drift to H_{cp}) of the panels, d_r, peak d_r values of 0.52% along X and 0.48% along Y at FDE, and 0.67% along X and 0.61% along Y at SDE come out for the most unfavourable hypothesis of column base constraint, α=10. These values are 7% greater than the ones obtained for α=∞ in X direction, and 15% greater in Y. At the same time, they are far below the 1% limitation adopted at the Immediate Occupancy (IO) performance level by [8], as well as by several other international Seismic Standards, for drift-sensitive non-structural elements not seismically interacting with the supporting structures, like the panels of the case study building. By considering that the maximum computed stress states of all columns are within their safe domains, the results of the analysis assess the attainment of IO performance level for structural members too, and thus for the building, up to the SDE.

The maximum drifts are equal to 2.35% in X and 1.96% in Y at BDE, and 3.03% in X and 2.51% in Y at MCE, for α=10. The differences with the results obtained for α=∞ are similar to the ones obtained for the FDE and SDE levels. For all α hypotheses, the peak d_r values correspond to severe distortions of the panel connections, with possible distributed cracking and spalling, as stressed by ASCE 41-06 Recommendations for the structural rehabilitation of existing buildings [14], at BDE. The drifts at MCE are only slightly lower than the values normally causing panels to fall down. Therefore, the response attained in current conditions can be identified with Life Safety (LS) non-structural performance level (corresponding to post-earthquake conditions that include significant — but non-life threatening — damage to non-structural components) at BDE, and Collapse Prevention (CP)

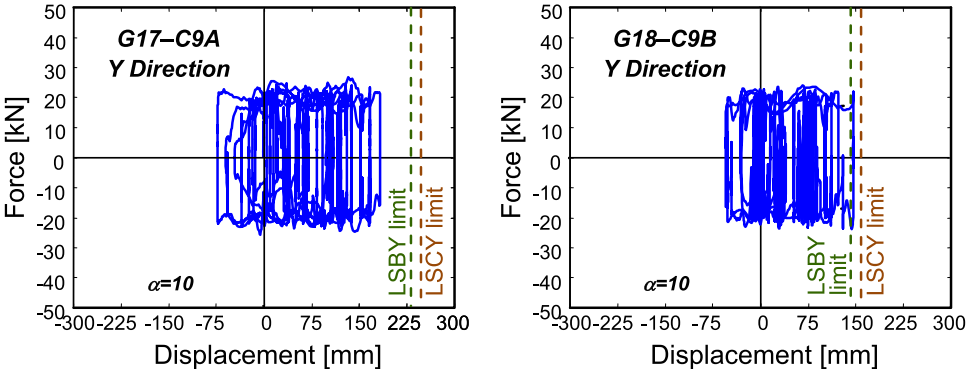

Fig. 7. Response cycles in Y direction of the neoprene-concrete contact elements situated between the left end of roof girders G17, G18 and the top section of columns C9A, C9B obtained from the most demanding MCE-scaled group of input accelerograms (LSBY limit=displacement value corresponding to loss of support from bearing in Y direction; LSCY limit=displacement value corresponding to loss of support from column in Y direction).

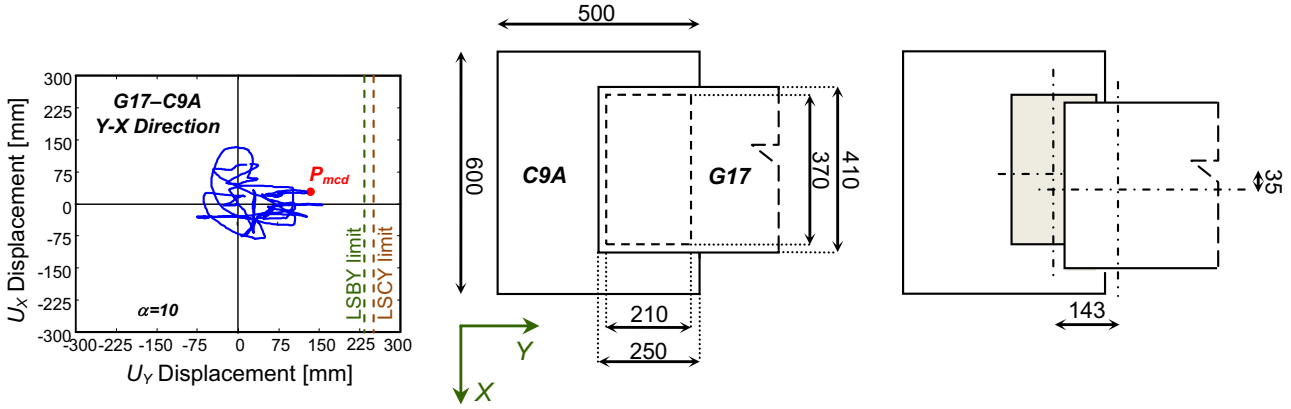

Fig. 8. Response trajectories of the left end section of roof girder G17 on top of column C9A obtained from the most demanding MCE-scaled group of input accelerograms (LSBY limit=displacement value corresponding to loss of support from bearing in Y direction; LSCY limit=displacement value corresponding to loss of support from column in Y direction); plan of the bearing zone; and representation of the condition of maximum combined displacement (point P_{mcd} in the graph).

non-structural performance level (corresponding to very severe damage to non-structural components, with small residual margin from falling) at MCE.

Concerning structural performance, the output displacements at MCE are examined to evaluate their effects on the stability of girders. Fig. 7 shows the response cycles in *Y* direction of the friction contact elements situated between the left end of girders G17, G18 and the top section of columns C9A, C9B obtained from the most demanding MCE-scaled group of input accelerograms, for α=10. The maximum displacements of these elements are equal to about 167 mm and 146 mm, respectively. The latter value is greater than the limit displacement of 140 mm causing loss of support of the G18 girder end section from the neoprene pad, and only 14 mm lower than the limit corresponding to the loss of support from the supporting column. The response is assessed further by examining the U_Y–U_X trajectories of the girder end sections, shown in Figs. 8 and 9. In the case of girder G17 (Fig. 8), although the maximum combined displacement condition — marked by point P_{mcd} in the graphs both of Figs. 8 and 9 — does not correspond to the geometrical loss of support from the bearing, the residual contact area with the neoprene pad is reduced to about 40% of its surface when P_{mcd} is attained. This transiently determines peak normal stresses on the residual contact area that are greater than the compressive strength of neoprene. Furthermore, during about one-sixth of the input ground motion duration (i.e. about 5 s), the contact area is reduced by about 50%. Therefore, critical response conditions of the girder end sections situated on the perimeter columns are noticed in terms of compressive stress demand for the neoprene bearings. The maximum deformed configuration in Fig. 9 confirms a negligible margin from fall of girder G18. The extremely narrow residual contact surface, limited to the concrete covers of the girder and the column, is subjected to unsafe compressive stresses too. The results for the other α values highlight loss of bearing support for α=15, and very little margins in the remaining cases (no greater than 11 mm for α=∞). Critical contact stress states come out for all α values. The maximum transient reduction of the contact area reaches 45% at BDE, with minimum margins of 35 mm from the loss-of-support limit.

The response of columns is checked in terms of biaxial flexure. By way of example of the results of the analysis at MCE, the $M_{lc,1}$–$M_{lc,2}$ biaxial moment interaction curves (being $M_{lc,1}$, $M_{lc,2}$ the bending moments around the local axes *1* and *2* of columns in plan, with *1* parallel to *X*, and *2* to *Y*) graphed by jointly plotting the two bending moment response histories obtained from the most demanding among the seven groups of MCE-scaled accelerograms, are plotted in Fig. 10 for columns C9A and C9B and α=10. The boundary of the $M_{lc,1}$–$M_{lc,2}$ safe interaction domain of columns traced out for the value of the axial force referred to the basic combination of gravity loads, named N_s in the following (equal to 295 kN for C9A and 515 kN for C9B), is also shown in the two graphs. The response curves highlight maximum $M_{lc,1}$–$M_{lc,2}$ combined values about 2.1 times greater than the corresponding values situated on the safe domain boundary, for column C9A, and about 2.05, for C2B. The stress states progressively grow as α does, with a maximum increase of 9% for α=∞.

For structural checks, Standards [8] impose a behaviour factor q=1.25 for isostatic precast concrete structures with no mechanical connectors capable of blocking the relative horizontal displacements between girders and columns, like in the case study. This strict

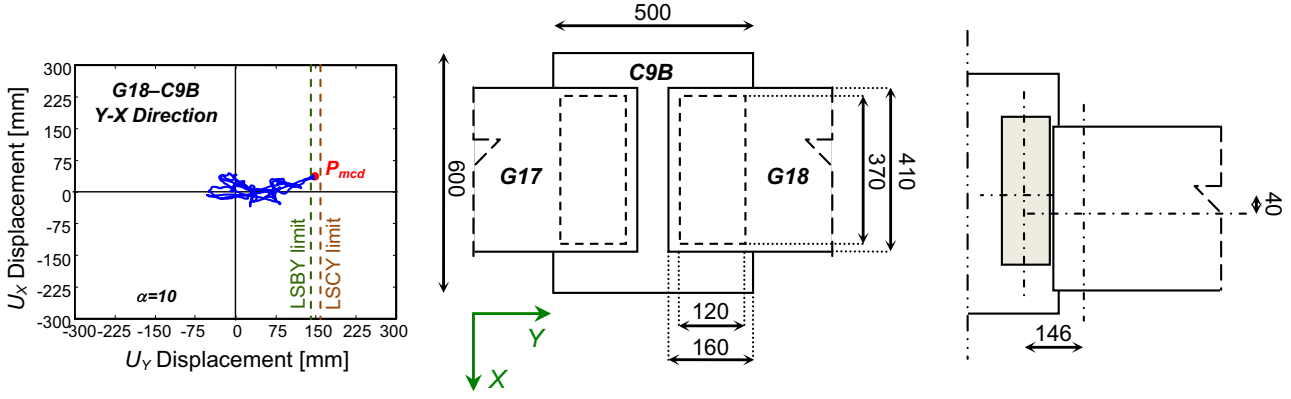

Fig. 9. Response trajectories of the left end section of roof girder G18 on top of column C9B obtained from the most demanding MCE-scaled group of input accelerograms (LSBY limit=displacement value corresponding to loss of support from bearing in Y direction; LSCY limit=displacement value corresponding to loss of support from column in Y direction); plan of the bearing zone; and representation of the condition of maximum combined displacement (point P_{mcd} in the graph).

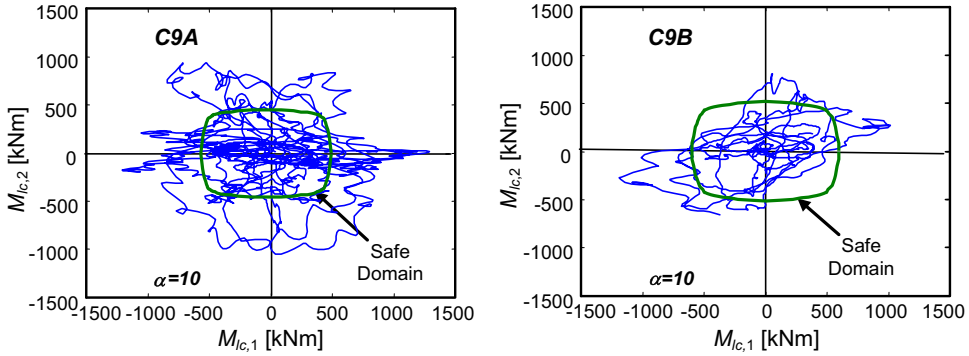

Fig. 10. $M_{lc,1}$–$M_{lc,2}$ interaction curves for columns C9A and C9B obtained from the most demanding MCE-scaled group of input accelerograms.

prescription on q can be by-passed by adding connectors, which could be easily planned within a traditional retrofit intervention on the building. However, a behaviour factor no greater than 1.5 should be adopted even after this intervention, considering that all remaining structural joints and details do not meet the design prescriptions of [8]. Therefore, even following this simple retrofit measure, the response stress states will be reduced at most by q=1.5, which does not allow the biaxial bending response of columns to pass the structural checks at the MCE too. The same occurs at the BDE, for which the stress states are approximately 20% lower, because some peak values of the $M_{lc,1}$–$M_{lc,2}$ interaction curves scaled by q=1.5 fall outside the safe domains of columns even for this earthquake level.

The poor performance evaluated in terms of both girder displacements/panel drifts and column strength prompted to extend the verification analysis to the inelastic field, so as to carefully assess the critical aspects highlighted by the elastic model response, and estimate the ductility demand on columns. The latter makes useful additional information, since the results of the strength checks discussed above are related to the choice of q, normatively determined by rules concerning the connections of structural and non-structural members, rather than by the ductility resources of columns. A synthesis of the plastic analyses is reported in the next Section.

4.3. Time-history verification and performance assessment analysis – Plastic model of columns

The plastic behaviour of columns was simulated by incorporating axial force–biaxial bending moment fiber-type plastic hinges at their bottom-end sections. The fiber hinge model included in the library of SAP2000NL subdivides the cross section of a frame element into a set of axial fibers, each of which is defined by a geometrical location, a tributary area and a stress-strain curve. The axial stresses are integrated over the section to compute the values of the axial force and the $M_{lc,1}$, $M_{lc,2}$ bending moments around the two local reference axes. The corresponding axial displacement and the rotations around the two axes are used to calculate the axial strains in each fiber.

The model mesh generated for the analysis, displayed in Fig. 11, is composed of 255 equal concrete fibers, with sides of 41.1 mm and 40 mm along axes *1* and *2*, and 12 steel fibers, representative of the 4 Ø20+8 Ø16 reinforcing bars. The cyclic stress-strain relationships assigned to concrete and steel, corresponding to the mechanical properties of the materials mentioned in Section 2, are also traced out in Fig. 11.

As expected, the results of the analysis highlight a noticeable inelastic demand for all columns. The $M_{lc,1}$–θ and $M_{lc,2}$–θ moment–rotation response cycles around axes *1* and *2* of column C9A are demonstratively plotted in Fig. 12, for the same input accelerogram Figs. 7–10 are referred to, and α=10. The maximum total rotation is equal to about 0.015 rad around *1*, and 0.017 rad around *2*. The plastic rotation, θ_{pl}, obtained by subtracting the elastic component from the total rotation, shows maximum values, $\theta_{pl,max}$, ranging from 0.013 rad (α=∞) to 0.011 rad (α=10) at the BDE, and from 0.017 rad (α=∞) to 0.015 rad (α=10) at the MCE. According to the criteria suggested in [14] with regard to the limit plastic rotation angles of R/C columns at the LS and CP performance levels, $\theta_{pl,lim,LS}$ and $\theta_{pl,lim,CP}$, the following values can be assumed by referring to the axial stress, mechanical, geometrical and reinforcement characteristics of the examined elements: $\theta_{pl,lim,LS}$=0.015 rad, and $\theta_{pl,lim,CP}$=0.02 rad. Therefore, based on the $\theta_{pl,max}$ values obtained from the inelastic analysis, the performance of columns is assessed by the attainment of LS level at BDE, and CP at MCE. It can be noted that this performance would be evaluated by the results of the elastic analysis should a q value nearly equal to 2 be adopted.

The E_i input, E_h hysteretic (i.e. dissipated by the plastic hinges) and E_m modal energy plus E_f friction (i.e. dissipated by the neoprene pads) energy time-histories of the structure obtained for the group of the most demanding input motions, automatically computed by the finite element software in the analysis, are plotted in Fig. 12 too. The energy balance at the end of the analysis highlights about 78% and 22% contributions of E_h and E_m+E_f dissipated energies, respectively. Similar results are found for the remaining groups of accelerograms.

As a consequence of the plastic rotations of the bottom end sections of columns, the maximum displacements of their top sections, and thus of the supported girders, increase by about 5% in X and 6.5% in Y at the BDE, and by about 7% in X and 9% in Y at the MCE, as compared to the elastic analyses. The MCE-related values identify a potential loss of support of girders from the internal columns, in addition to the loss of support from the neoprene pads assessed by the analysis in the hypothesis of elastic behaviour of columns.

By recapitulating the results of the assessment study in current conditions, the following performance level–earthquake level correlations are found for structural and non-structural elements: IO–FDE, IO–SDE and LS–BDE. CP is attained for columns and non-structural elements at MCE, whereas loss of support of roof girders from the neoprene pads is evaluated by the elastic analysis, and from some central columns by the plastic analysis. The latter configuration corresponds to the structural collapse of the roof.

The stress state checks on the foundation plinths and the underlying soil, which were examined separately in order to limit the dimensions of the finite element model in the time-history computations, are passed up to the MCE input level.

5. Supplemental damping-based retrofit hypothesis

Supplemental damping-based technologies have been increasingly adopted in the last decades as seismic retrofit strategies [15,16], and they now represent a well-established and cost-effective alternative to traditional rehabilitation measures. This is also demonstrated by the latest achievements in this field, regarding systems incorporating viscous [17–27], metallic yielding [28–30] or friction [31] dissipaters,

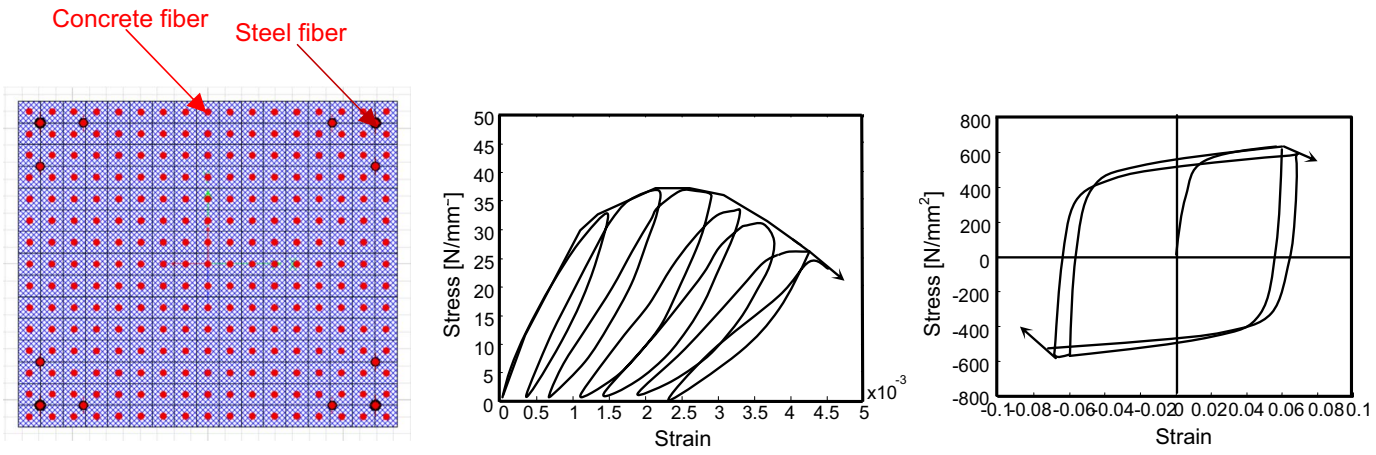

Fig. 11. Fiber model of the cross section of columns and stress-strain relationships for concrete and reinforcing steel.

as well as buckling-restrained [22,32] and other innovative layouts of steel braces [33–37].

The retrofit hypothesis developed here is based on the adoption of a dissipative bracing system incorporating pressurized fluid viscous (FV) spring-dampers, originally conceived and implemented by the authors for installation in frame buildings [38–40]. Application to the seismic retrofit of hall-type prefab R/C structures is examined for the first time in this study. Detailed information on the mechanical properties of the FV devices is provided in [38–40]. Concerning their analytical/numerical modelling, the time-dependent F_d damping and F_{ne} non-linear elastic reaction forces corresponding to the damper and spring function are effectively simulated by the following expressions [41]:

$$F_d(t) = c\,\mathrm{sgn}(\dot{x}(t))|\dot{x}(t)|^{\gamma} \tag{4}$$

$$F_{ne}(t) = k_2 x(t) + \frac{(k_1 - k_2)\,x(t)}{\left[1 + \left|\frac{k_1 x(t)}{F_0}\right|^5\right]^{1/5}} \tag{5}$$

where t=time variable; c=damping coefficient; sgn(·)=signum function; $\dot{x}(t)$=device velocity; |·|=absolute value; γ=fractional exponent, ranging from 0.1 to 0.2; F_0=static pre-load force; k_1, k_2=stiffness of the response branches situated below and beyond F_0; and $x(t)$=device displacement.

As shown by the building plan in Fig. 13, the dissipative braces are placed in six alignments parallel to X (named *Al. X1* through *Al. X6*) and six alignments parallel to Y (*Al. Y1–Al. Y6*). The former are constituted by pairs of adjacent columns belonging either to the perimeter column lines (*Al. X1*, *Al. X2*, *Al. X5*, *Al. X6*) or to the central column line (*Al. X3*, *Al. X4*). Concerning the Y-parallel alignments, because the girder span is about 20 m long, six columns made of HEB300 steel profiles, named AC1 through AC6 in Fig. 13, are added at the mid-span prior to mounting the bracing members.

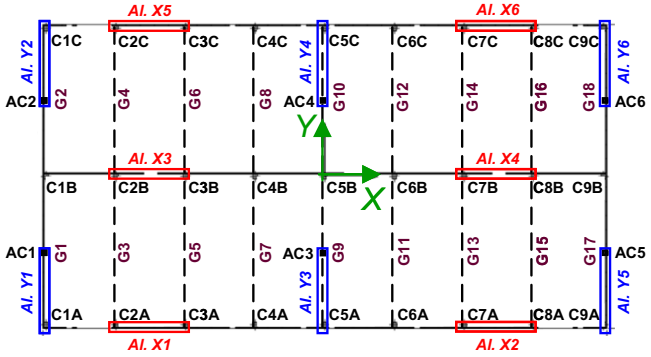

Fig. 13. Vertical alignments selected for the installation of the supplemental damping system.

The installation layout of the FV springs-dampers is identical to the basic configuration devised for frame buildings [38–40], where a pair of interfaced devices is placed in parallel with the connecting beam axis, at the tip of each couple of supporting braces (Fig. 14). The connecting beams are made of HEB300 steel profiles, and the braces of tubular profiles, 219.1 mm wide and 6.3 mm thick.

The design of the FV devices is developed by the general criterion formulated in [38], which consists in assigning the set of installed devices the capability of dissipating a prefixed energy fraction, $E_{d,t}$, of the maximum seismic input energy computed by the numerical model of the structure. $E_{d,t}$ is calibrated depending on the design objectives assumed case by case. For the examined building, an elastic response is targeted up to the maximum considered earthquake, in view of the relatively low ductility of columns. In order to reach this objective, by referring to the suggestions formulated for frame structures [38–40],

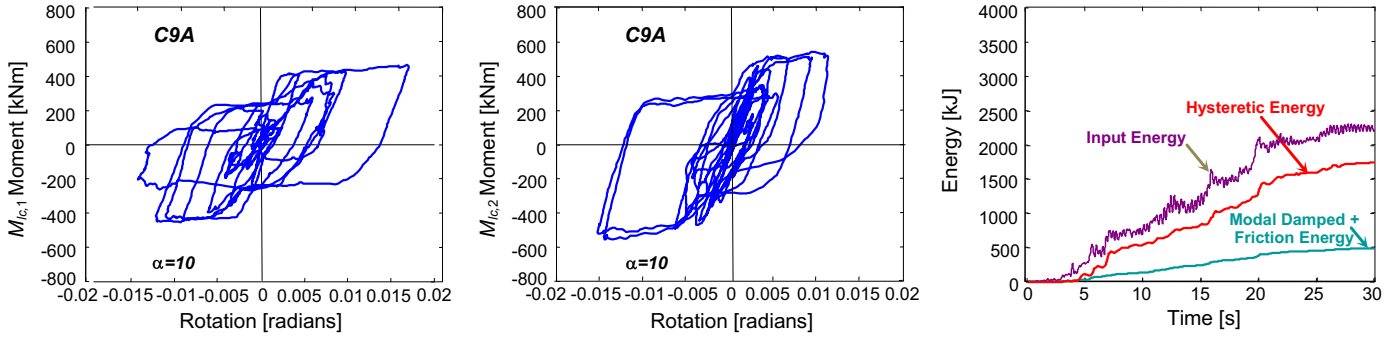

Fig. 12. Response cycles around local axes *1* and *2* of the plastic fiber hinge at the base of column C9A, and energy time-histories of the structure obtained from the most demanding MCE-scaled group of input accelerograms.

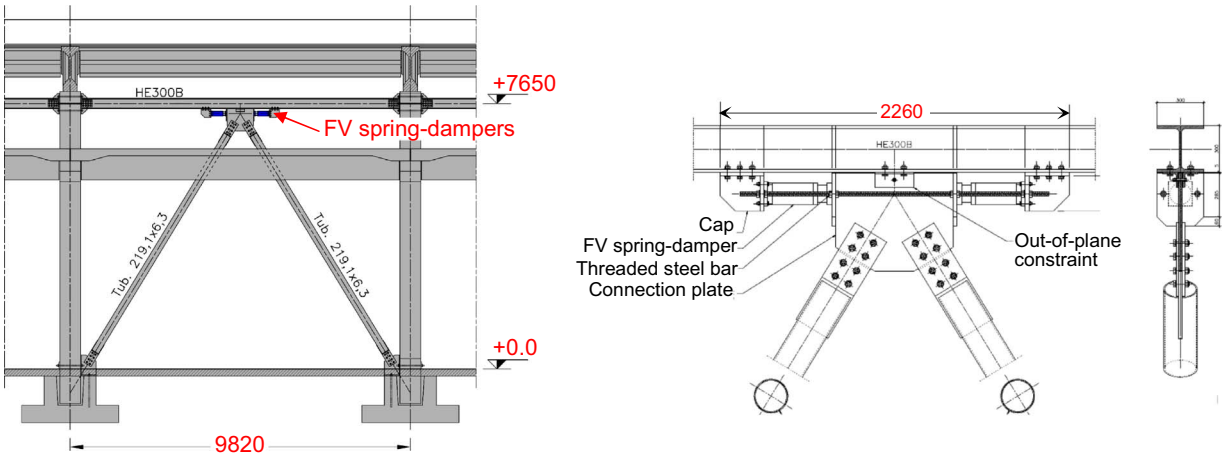

Fig. 14. Installation details of the supplemental damping system in the perimeter alignments.

$E_{d,t}$ is tentatively fixed at 80% of the input energy calculated for the response to the MCE-scaled input action. The $E_{d,t}$ demand estimated by this criterion is met by a set of medium-sized FV spring-dampers in current production [42], characterised by a nominal energy dissipation capacity, E_n, equal to 50 kJ, and a stroke, x_{max}, of ± 60 mm.

The finite element model of the structure incorporating the protective system is shown in Fig. 15. For the development of the numerical analyses, the FV spring-damper model is obtained by combining in parallel a non-linear dashpot and a non-linear spring with reaction forces given by expressions (4) and (5) [38]. A new modal analysis carried out in retrofitted conditions highlights the same sequence of four main modes as in the original structure, i.e. with the first and third mode purely translational along *X* and *Y*, respectively, and the second and fourth mode purely rotational around *Z*. As a result of the stiffening action of the dissipative bracing system, the values of the vibration periods in the hypothesis of fixed-end columns are reduced as follows: first mode – 1.33 s (instead of 1.69 s); third mode – 1.13 s (instead of 1.31 s); second and fourth mode – 1.07 s and 0.95 s (instead of 1.38 s and 1.24 s). At the same time, the EMMs are substantially unchanged as compared to the original structure. The influence of the stiffness modulation coefficient α on the period values is practically the same as in unprotected conditions, as discussed in Section 3.2 and highlighted in Fig. 4 above.

The results of the time-history verification analyses in rehabilitated configuration are synthesized in Figs. 16–18, all referred to the response induced by the most demanding of the seven groups of input ground motions scaled at the MCE level, and α=10.

The $M_{lc,1}$–$M_{lc,2}$ interaction curves and $M_{lc,1}$–θ response cycles of the base section of column C9A, plotted in Figs. 10 and 12 above for the original structure, are duplicated in Fig. 16 in retrofitted conditions. The first graph in Fig. 16 shows that the protective action of the supplemental damping system allows confining the interaction curves within the biaxial moment safe domain; the second graph displays a response of the plastic fiber hinge limited to the elastic branch. The same performance is surveyed for all remaining columns, assessing the attainment of the target objective represented by an elastic structural response up to the MCE.

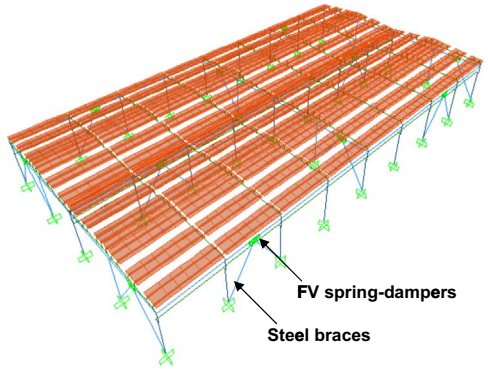

Fig. 15. View of the finite element model incorporating the supplemental damping system.

The U_X displacement time-histories of the left end section of roof girder G17 illustrated in Fig. 17 show a reduction factor equal to about 6 when passing from original to retrofitted conditions, which corresponds to a drop of the peak drift ratio of panels from 3.03% to 0.51%. The latter value virtually coincides with the maximum d_r value obtained in original configuration at the FDE, far below the IO-related 1% drift limitation. The remarkable reduction in displacements is a consequence of the very high damping capability of this class of dissipaters, owed to the low values of the fractional exponent γ in Eq. (4), as observed in previous studies concerning the applications in different building types [38–40].

The total reaction force–displacement $[(F_d(t)+F_{ne}(t)]$–$x(t)$ response cycles of the pairs of FV devices situated in the *Al. X4* and *Al. Y4* alignments are visualized in Fig. 18. The cycles exhibit peak displacements below the available stroke limit of ± 60 mm, which guarantees an uninterrupted functioning of the spring-dampers throughout the input motion duration. The energy time-histories plotted in the left graph in Fig. 18 assess that the energy dissipated by the FV elements is nearly equal to the targeted 80% of the input energy. Similar results are obtained for the other input accelerograms, as well as for $\alpha > 10$.

Finally, it is observed that the additional stress states transferred by the braces to the foundation plinths are offset by the remarkably reduced values transmitted by the columns, thanks to the supplemental damping action of the protective system. This results in safe stress states in retrofitted conditions too, and allows avoiding any strengthening intervention on the foundation members.

6. Conclusions

The remarkable seismic vulnerability of prefab R/C buildings designed with older Technical Standards, repeatedly highlighted during recent earthquakes, was formally assessed for a representative structure in this study.

The girder-to-column frictional contact, the possible rigid rotation of the bottom ends of columns and their plastic behaviour were simulated in the finite element analyses, so as to obtain a detailed evaluation of the seismic performance of the building at the four normative earthquake levels adopted in the current Italian Standards.

Substantially greater performance was achieved thanks to a supplemental damping-based retrofit strategy incorporating FV spring-dam-

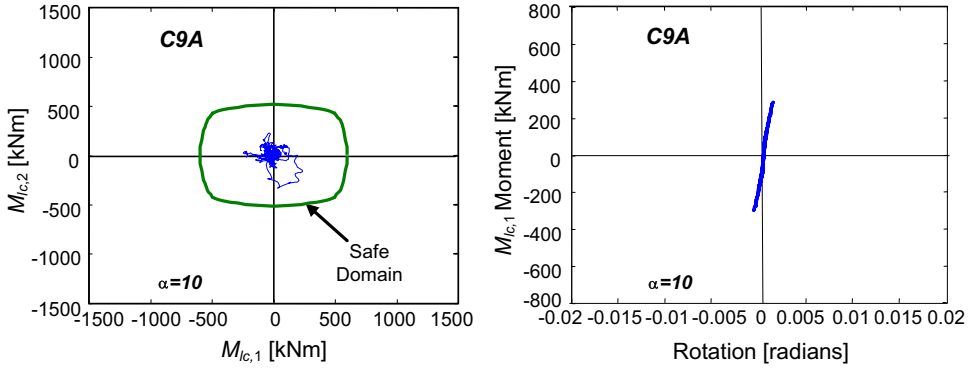

Fig. 16. $M_{lc,1}$–$M_{lc,2}$ interaction curves and $M_{lc,1}$–θ response graph for column C9A obtained from the most demanding MCE-scaled group of input accelerograms in retrofitted conditions.

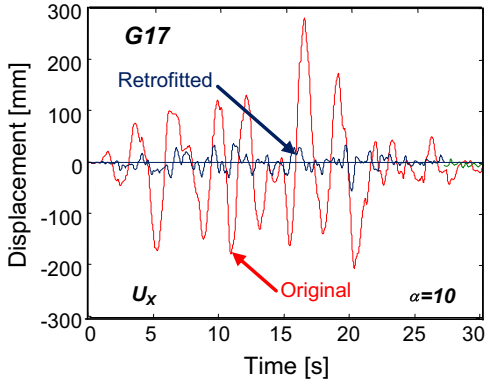

Fig. 17. Displacement time-histories in *X* direction of the left end section of roof girder G17 obtained from the most demanding MCE-scaled group of input accelerograms in retrofitted and original conditions.

pers. This strategy had already been applied to other types of structures in previous studies by the authors, and was implemented in prefab R/C buildings for the first time here.

Further specific remarks are summarised below.

– Little influence of the stiffness modulation coefficient α of the column base springs on the modal and time-history response is noticed up to α=10. As compared to this value, the results in fixed-end conditions are at most 15% greater in terms of stress states, and 15% lower in terms of displacements, also considering a plastic behaviour of columns. These data highlight that, for similar cases where the empirical fixed-end condition $h_e/s \geq 1.5$ is not met but the h_e/s ratio of column embedment depth to column side is at least equal to 1, the analysis can be simply carried out with conventional fixed-end constraints, and the displacement response conservatively amplified by about 15%. When $h_e/s < 1$ the flexibility of the column-base constraint should be carefully taken into account, like in this case study.
– The response at MCE level shows the possible loss of support of some girders from the neoprene pads situated on top of the central columns, or from the latter — which could cause the collapse of a roof portion — assuming either an elastic or a plastic behaviour of columns, respectively. Furthermore, the considerable reduction of the contact area with the pads determines a critical compressive stress demand for the material. Near-critical response conditions are noticed at the BDE.
– Remarkably unsafe conditions come out from the stress state checks of columns based on their elastic analysis, and a high plastic demand is consistently derived from the inelastic analysis. The corresponding structural performance is assessed by the attainment of Life Safety level at BDE, and Collapse Prevention level at MCE.
– The drifts computed for the cladding panels are capable of inducing distributed cracking and spalling along their surface, as well as severe distortions in their connections to the purlins, at BDE. The drifts at MCE are only slightly lower than the values normally causing panels to fall down. As a consequence, the non-structural performance–earthquake level correlations are the same as for the structural members, i.e. LS–BDE and CP–MCE.
– The incorporation of a supplemental damping protective system allows reaching an elastic and safe response of all structural and non-structural members. A drop in drifts approximately equal to 6 is particularly surveyed at MCE. This allows attaining the Immediate Occupancy level up to MCE, i.e. the same performance obtained in original configuration at the FDE.
– The dissipative braces can be installed following the same mounting procedure and adopting the details devised for frame structures. The retrofit intervention is limitedly invasive, as only two brace pairs are introduced in internal alignments along *X*, and two along *Y*. No strengthening intervention is required on the foundation members.

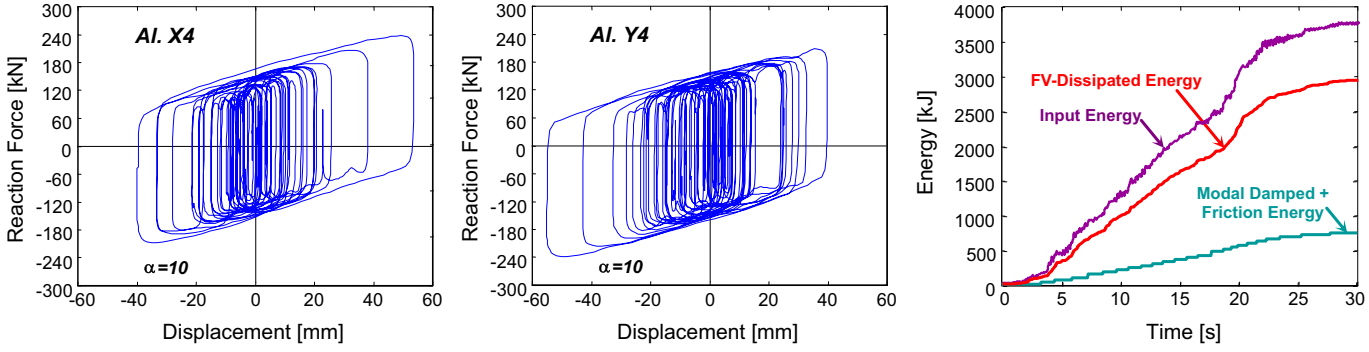

Fig. 18. Response cycles of the spring-damper pairs incorporated in alignments *X4* and *Y4*, and energy time-histories of the structure obtained from the most demanding MCE-scaled group of input accelerograms in retrofitted conditions.

Acknowledgements

The study reported in this paper was sponsored by the Italian Department of Civil Protection within the ReLUIS-DPC Project 2014/2016, research Line 6: Isolation and Dissipation. The authors gratefully acknowledge this financial support.

References

[1] Mitchell D, DeVall R, Saatcioglu M, Simpson R, Tinawi R, Tremblay R. Damage to concrete structures due to the 1994 Northridge earthquake. Can J Civ Eng 1995;22:361–77.
[2] Sezen H, Whittaker AS. Seismic performance of industrial facilities affected by the1999 Turkey Earthquake. J Perform Constr Facil 2006;20:28–36.
[3] Saatcioglu M, Mitchell D, Tinawi R, Gardner NJ, Gillies AG, Ghobarah A, Anderson DL, Lau D. The August 17, 1999, Kocaeli (Turkey) earthquake — damage to structures. Can J Civ Eng 2001;28:715–37.
[4] Arslan MH, Korkmaz H, Gülay FG. Damage and failure pattern of prefabricated structures after major earthquakes in Turkey and shortfalls of the Turkish Earthquake Code. Eng Fail Anal 2006;2006(13):537–57.
[5] Toniolo G, Colombo A. Precast concrete structures: the lessons learned from the L'Aquila earthquake. Struct Concr 2012;13:73–83.
[6] Magliulo G, Ercolino M, Petrone C, Coppola O, Manfredi G. The Emilia Earthquake: seismic performance of precast reinforced concrete buildings. Earthq Spectra 2014;30:891–912.
[7] Bournas DA, Negro P, Taucer F. Performance of industrial buildings during the Emilia earthquakes in Northern Italy and recommendations for their strengthening. Bull Earthq Eng 2014;12:2383–404.
[8] Technical Standards on Constructions. Italian Council of Public Works; Rome, Italy. 2008. [in Italian].
[9] SAP2000NL . Theoretical and users' manual. Release 17.11. Berkeley, CA: Computers & Structures Inc.; 2015.
[10] Osanai Y, Watanabe F, Okamoto S. Stress transfer mechanism of socket base connection with precast concrete columns. ACI Struct J 1996;93:266–76.
[11] Wald F. Influence of the column base stiffness on sway frames. COST C1 Control of the semi-rigid behaviour of civil engineering structural connections, Doc. C1/WD2/96-12. Aachen, Germany; 1996.
[12] Magliulo G, Capozzi V, Fabbrocino G, Manfredi G. Neoprene–concrete friction relationships for seismic assessment of existing precast buildings. Eng Struct 2011;33:532–8.
[13] Vanmarcke EH, Fenton GA, Heredia-Zavoni E. SIMQKE-II – Conditioned earthquake ground motion simulator: user's manual, version 2.1. Princeton, NJ: Princeton University; 1999.
[14] ASCE/SEI 41-06 . Seismic rehabilitation of existing buildings. Reston, VA: American Society of Civil Engineers – Structural Engineering Institute; 2006.
[15] Constantinou MC, Soong TT, Dargush GF. Passive energy dissipation systems for structural design and retrofit. Monograph series No. 1. Buffalo, NY: MCEER; 1998.
[16] Christopoulos C, Filiatrault A. Principles of passive supplemental damping and seismic isolation. Pavia, Italy: IUSS Press; 2006.
[17] He X, Chen W, Zhu B. Theoretical analysis on the damping characteristics of a clearance type viscous damper. Adv Sci Lett 2012;15:422–4.
[18] Weng DG, Zhang C, Lu XL, Zeng S, Zhang SM. A simplified design procedure for seismic retrofit of earthquake-damaged RC frames with viscous dampers. Struct Eng Mech 2012;44:611–31.
[19] Landi L, Lucchi S, Diotallevi PP. A procedure for the direct determination of the required supplemental damping for the seismic retrofit with viscous dampers. Eng Struct 2014;71:137–49.
[20] Guo T, Xu J, Xu W, Di Z. Seismic upgrade of existing buildings with fluid viscous dampers: design methodologies and case study. J Perform Constr Facil 2015;2015:29, 04014175.
[21] Losanno D, Spizzuoco M, Serino G. An optimal design procedure for a simple frame equipped with elastic-deformable dissipative braces. Eng Struct 2015;101:677–97.
[22] Magar Patil HR, Jangid RS. Numerical study of seismic performance of steel moment-resisting frame with buckling-restrained brace and viscous fluid damper. IES J Part A: Civ Struct Eng 2015;8:165–74.
[23] Saha A, Saha P, Patro SK. Seismic response control of benchmark highway bridge using non-linear FV spring damper. IES J Part A: Civ Struct Eng 2015;8:240–50.
[24] Cancellara D, De Angelis F. Nonlinear dynamic analysis for multi-storey RC structures with hybrid base isolation systems in presence of bi-directional ground motions. Compos Struct 2016;154:464–92.
[25] Dong B, Sause R, Ricles JM. Seismic response and performance of a steel MRF building with nonlinear viscous dampers under DBE and MCE. ASCE J Struct Eng 2016;2016:142, 04016023.
[26] Høgsberg J, Brodersen ML. Hybrid viscous damper with filtered integral force feedback control. J Vib Control 2016;22:1645–56.
[27] Palermo M, Silvestri S, Landi L, Gasparini G, Trombetti T. Peak velocities estimation for a direct five-step design procedure of inter-storey viscous dampers. Bull Earthq Eng 2016;14:599–619.
[28] Ponzo FC, Di Cesare A, Nigro D, Vulcano A, Mazza F, Dolce M, Moroni C. JET-PACS project: dynamic experimental tests and numerical results obtained for a steel frame equipped with hysteretic damped chevron braces. J Earthq Eng 2012;16:662–85.
[29] Mazza F, Vulcano A. Equivalent viscous damping for displacement-based seismic design of hysteretic damped braces for retrofitting framed buildings. Bull Earthq Eng 2014;12:2797–819.
[30] Mazza F. Displacement-based seismic design of hysteretic damped braces for retrofitting in-plan irregular r.c. framed structures. Soil Dyn Earthq Eng 2014;66:231–40.
[31] Hu JW, Noh M. Seismic response and evaluation of SDOF self-centering friction damping braces subjected to several earthquake ground motions. Adv Mater Sci Eng 2015, 397273.
[32] Gu Q, Zona A, Peng Y, Dall'Asta A. Effect of buckling-restrained brace model parameters on seismic structural response. J Constr Steel Res 2014;98:100–13.
[33] Ozcelik R, Binici B, Kurc O. Pseudo dynamic test of a deficient reinforced concrete frame upgraded with internal steel frames. Earthq Eng Struct Dyn 2013;42:763–78.
[34] Ju M, Lee KS, Sim J, Kwon H. Non-compression X-bracing system using CF anchors for seismic strengthening of RC structures. Mag Concr Res 2014;66:159–74.
[35] Huang L, Tan H, Yan L. Seismic behavior of chevron braced reinforced concrete spatial frame. Mater Struct 2015;48:4005–18.
[36] Fanaie N, Aghajani S, Dizaj EA. Theoretical assessment of the behavior of cable bracing system with central steel cylinder. Adv Struct Eng 2016;19:463–72.
[37] Mazza F. Comparative study of the seismic response of RC framed buildings retrofitted using modern techniques. Earthq Struct 2015;9:29–48.
[38] Sorace S, Terenzi G. Seismic protection of frame structures by fluid viscous damped braces. ASCE J Struct Eng 2008;134:45–55.
[39] Sorace S, Terenzi G. Dissipative bracing-based seismic retrofit of R/C school buildings. Open J Constr Build Technol 2012;6:334–45.
[40] Sorace S, Terenzi G. Motion control-based seismic retrofit solutions for a R/C school building designed with earlier Technical Standards. Bull Earthq Eng 2014;12:2723–44.
[41] Sorace S, Terenzi G. Non-linear dynamic modelling and design procedure of FV spring-dampers for base isolation. Eng Struct 2001;23:1556–67.
[42] Jarret SL. Shock-control technologies. URL ⟨http://www.introini.info⟩; 2016.